BIOCHEMISTRY
including biophysical chemistry & molecular biology
Article

Biochemistry **2010,** *49,* 10623–10635 10623
DOI: 10.1021/bi101389r

Major Antiparallel and Minor Parallel β Sheet Populations Detected in the Membrane-Associated Human Immunodeficiency Virus Fusion Peptide[†]

Scott D. Schmick and David P. Weliky*

Department of Chemistry, Michigan State University, East Lansing, Michigan 48824, United States

Received August 27, 2010; Revised Manuscript Received November 11, 2010

ABSTRACT: The HIV gp41 protein catalyzes fusion between viral and host cell membranes, and its apolar N-terminal region or "fusion peptide" binds to the host cell membrane and plays a key role in fusion. "HFP" is a construct containing the fusion peptide sequence, induces membrane vesicle fusion, and is an important fusion model system. Earlier solid-state nuclear magnetic resonance (SSNMR) studies showed that when HFP is associated with membranes with ∼30 mol % cholesterol, the first 16 residues have predominant β strand secondary structure and a fraction of the strands form antiparallel β sheet structure with residue 16→1/1→16 or 17→1/1→17 registries for adjacent strands. In some contrast, other SSNMR and infrared studies have been interpreted to support a large fraction of an approximately in-register parallel registry of adjacent strands. However, the samples had extensive isotopic labeling, and other structural models were also consistent with the data. This SSNMR study uses sparse labeling schemes that reduce ambiguity in the determination of the fraction of HFP molecules with parallel β registry. Quantitative analysis of the data shows that the parallel fraction is at most 0.15 with a much greater fraction of antiparallel 16→1/1→16 and 17→1/1→17 registries. These data strongly support a model of HFP-induced vesicle fusion caused by antiparallel rather than parallel registries and provide insight into the arrangement of gp41 molecules during HIV−host cell fusion. This study is an example of quantitative determination of a complex structural distribution by SSNMR, including experimentally validated inclusion of natural abundance contributions to the SSNMR data.

AIDS is caused by membrane-enveloped human immunodeficiency virus (HIV)[1] that infects host cells by fusion, i.e., joining of viral and host cell membranes (*1*). Fusion is facilitated by gp41, which is an integral HIV membrane protein. The N-terminal ∼175-residue gp41 ectodomain lies outside the virus, and X-ray crystal and liquid-state nuclear magnetic resonance (LSNMR) structures of soluble regions of the ectodomain have shown molecular trimers (*1*−*5*). These structures lacked the ∼25-residue N-terminal "fusion peptide" region that plays a key role in fusion and infection as evidenced by inhibition of fusion and infection when gp41 had mutations within the fusion peptide region (*1*, *6*, *7*). Peptides with the fusion peptide sequence are denoted HFPs and have been studied as model fusion systems because they induce vesicle fusion and because their mutation−fusion activity relationships are similar to those of in vivo fusion and infection (*1*, *8*−*10*).

The HFP structure−function literature includes NMR data showing random coil structure for HFP in aqueous solution (*11*, *12*). Solid-state nuclear magnetic resonance (SSNMR) has shown predominant β sheet structure for residues 1−16 of membrane-associated HFP where the membranes contained ∼30 mol % cholesterol, which is comparable to the mole percent of cholesterol of membranes of HIV and host cells of HIV (*13*−*16*). A fluorescence and infrared (IR) study reported the time-resolved courses of HFP structural changes and the intervesicle lipid mixing function following addition of a HFP solution to a membrane vesicle solution (*17*). The experimental rates (R) were ordered $R_{\text{HFP membrane binding}} > R_{\text{HFP }\beta\text{ sheet formation}} > R_{\text{lipid mixing}}$ and were consistent with the following sequence: (1) random coil HFPs binding to a membrane vesicle, (2) HFP structure changing to oligomeric β sheet, and (3) vesicle fusion.

The biological relevance of HFP oligomers is further supported by the molecular trimer structure of soluble regions of the gp41 ectodomain (*3*−*5*). The region between residues T25 and G85 of each molecule was a continuous helix, and the helices of the different molecules formed a parallel coiled coil. The fusion peptide region was not included in the protein constructs for these structures but would be N-terminal of residue T25. A C-terminally cross-linked HFP trimer (HFPtr) was therefore synthesized to mimic the close proximity of the three T25 residues in the coiled coil. Relative to the HFP monomer, HFPtr induced membrane vesicle fusion with an ∼40-fold faster rate, which supported the functional significance of the trimer (*18*). Although both the monomer and trimer formed β sheet oligomers in membranes with cholesterol, HFPtr is more deeply inserted, which correlates with greater membrane perturbation and a reduction of the vesicle fusion activation energy (*19*). The in vivo importance of fusion peptide oligomers was also demonstrated by dominant inhibition of fusion and infection in viruses and cells for which

[†]This work was supported by National Institutes of Health Grant AI47153 to D.P.W.

*To whom correspondence should be addressed. Telephone: (517) 355-9715. Fax: (517) 353-1793. E-mail: weliky@chemistry.msu.edu.

[1]Abbreviations: CO, carbonyl; *d*, magnetic dipole−dipole coupling; DTPC, 1,2-di-*O*-tetradecyl-*sn*-glycero-3-phosphocholine; DTPG, 1,2-di-*O*-tetradecyl-*sn*-glycero-3-phospho-*rac*-(1-glycerol) sodium salt; FMOC, 9-fluorenylmethoxycarbonyl; HEPES, *N*-(2-hydroxyethyl)piperazine-*N*′-2-ethanesulfonic acid; HFP, HIV fusion peptide; HFPtr, HIV fusion peptide trimer; HIV, human immunodeficiency virus; IR, infrared; MAS, magic angle spinning; max nad, maximum natural abundance dephasing; min nad, minimum natural abundance dephasing; na, natural abundance; nad, natural abundance dephasing; NMR, nuclear magnetic resonance; PDB, Protein Data Bank; *r*, internuclear distance; REDOR, rotational-echo double resonance; SIMPSON, simulation program for solid-state NMR spectroscopy; SSNMR, solid-state NMR; TFA, trifluoroacetic acid; TPPM, two-pulse phase modulation.

Published on Web 11/15/2010

(a) Peptides

```
                1         10         20         30
HFP-F8          AVGIGALFLGFLGAAGSTMGARSWKKKKKKA
HFP-L12         AVGIGALFLGFLGAAGSTMGARSWKKKKKKA
HFP-G5A6        AVGIGALFLGFLGAAGSTMGARSWKKKKKKA
HFP-A6L7        AVGIGALFLGFLGAAGSTMGARSWKKKKKKA
HFP-L12G13      AVGIGALFLGFLGAAGSTMGARSWKKKKKKA
HFP-G13A14      AVGIGALFLGFLGAAGSTMGARSWKKKKKKA
```

(b) Samples

HFP-NC	HFP-F8 + HFP-A6L7	(1:2)
HFP-P	HFP-L12/HFP-G13A14	(1:2)
HFP-A	HFP-L12/HFP-G5A6	(1:2)
HFP-AP	HFP-F8/HFP-L9G10	(1:2)

(c) Registries

	Parallel 1→17/1→17	Parallel 2→17/1→16	Antiparallel 16→1/1→16	Antiparallel 17→1/1→17
HFP-P	AVGIGALFLGFLGAAGS AVGIGALFLGFLGAAGS	AVGIGALFLGFLGAAGS AVGIGALFLGFLGAAGS	SGAAGLFGLFLAGIGVA AVGIGALFLGFLGAAGS	SGAAGLFGLFLAGIGVA AVGIGALFLGFLGAAGS
HFP-A	AVGIGALFLGFLGAAGS AVGIGALFLGFLGAAGS	AVGIGALFLGFLGAAGS AVGIGALFLGFLGAAGS	SGAAGLFGLFLAGIGVA AVGIGALFLGFLGAAGS	SGAAGLFGLFLAGIGVA AVGIGALFLGFLGAAGS
HFP-AP	AVGIGALFLGFLGAAGS AVGIGALFLGFLGAAGS	AVGIGALFLGFLGAAGS AVGIGALFLGFLGAAGS	SGAAGLFGLFLAGIGVA AVGIGALFLGFLGAAGS	SGAAGLFGLFLAGIGVA AVGIGALFLGFLGAAGS

FIGURE 1: (a) HFPs for which red and blue correspond to ^{13}CO- and ^{15}N-labeled residues, respectively. (b) HFP-NC, HFP-P, HFP-A, and HFP-AP were SSNMR samples that each contained a mixture of ^{13}CO- and ^{15}N-labeled peptides in a 1:2 molar ratio. The HFP-NC sample was a mixture of HFP-F8 and HFP-A6L7 that had been lyophilized separately. The other samples were membrane-associated HFPs that formed β sheet structure with a molecular mixture of ^{13}CO- and ^{15}N-labeled peptides in the sample. (c) Registries probed by the SSNMR REDOR experiments and labeled ^{13}CO/labeled ^{15}N proximities for the membrane-associated HFPs in these registries. Consideration of residue 1→16 or 1→17 registries is based on the fully extended conformation of this HFP region. For parallel sheets, there is CO(residue i)−HN(residue $i+1$) hydrogen bonding of adjacent strands.

a small fraction of the gp41 had the V2E point mutation in the fusion peptide region (*7*, *20*). Analyses of these data supported the involvement of multiple gp41 trimers and fusion peptides in fusion (*21*). Electron micrographs of virus−cell contacts have also been interpreted to show multiple gp41 trimers at the contact site (*22*). The functional importance of fusion peptide trimers has also been demonstrated for fusion peptides of other viruses (*23*, *24*).

Because of the aforementioned functional significance of HIV fusion peptide oligomers, there has been an effort to elucidate the distribution of structures of membrane-associated HFP oligomers. SSNMR has played a key role in this effort, in particular for samples prepared in a manner similar to that of fusion assays with addition of an aqueous fusion peptide solution to a membrane vesicle solution (*14*). Appendage of a C-terminal lysine tag to HFP greatly reduced the level of HFP aggregation in aqueous solution and allowed separation of pelleted fused vesicles with bound HFP from unbound HFP in the supernatant (*12*, *18*, *25*). HFP−lipid binding was supported by SSNMR detection of a HFP A1 ^{13}CO(carbonyl)−lipid ^{31}P distance of ~5 Å (*19*). For membrane-associated HFP, the ^{13}C chemical shifts derived from an unambiguous assignment were consistent with a fully extended β strand conformation for residues between A1 and G16 (*15*). Detection of intermolecular ^{13}C−^{13}C and ^{13}C−^{15}N distances of ~5 Å supported β sheet oligomer/aggregate structure, and the A1 ^{13}CO−lipid ^{31}P contact and other data suggest that the number of molecules in the oligomer is small (*15*, *19*, *26*).

This work focuses on the quantitative determination of populations of specific β sheet registries. The clearest information to date on this topic has been a SSNMR experiment with membrane-associated HFP with an A14 ^{13}CO label and a G3 ^{15}N label whose separation (r_{CN}) was >20 Å along a single β strand (*15*). SSNMR can detect labeled ^{13}CO−^{15}N dipolar coupling (d_{CN}) where $d_{CN} = 3109/r_{CN}^3$, with d in hertz and r in angstroms. The minimum detectable d_{CN} (≈10 Hz) correlates with an r_{CN} of ≈7 Å, so that detectable d_{CN} values in this sample were necessarily ascribed to inter- rather than intramolecular ^{13}CO−^{15}N proximity. SSNMR detection of >30 Hz d values strongly supported a significant fraction of molecules with intermolecular A14−G3 hydrogen bonding and labeled r_{CN} values of 4.1 and 5.5 Å, i.e., 16→1/1→16 antiparallel β sheet registry. Figure 1c displays this registry with isotopic labeling from this study and not the earlier study. Detection of similarly large d values in an A14 ^{13}CO−I4 ^{15}N HFP sample supported a fraction of 17→1/1→17 antiparallel registry.

At most, half of the membrane-associated HFP molecules were in the 16→1/1→16 or 17→1/1→17 registries; i.e., a large fraction of the molecules were in registries not detected in either the A14 ^{13}CO/G3 ^{15}N or A14 ^{13}CO/I4 ^{15}N labeled samples. Because of the proximity of the T25 residues of the three molecules of the gp41 trimer, a reasonable hypothesis for a populated HFP registry is in-register parallel β sheet, i.e., 1→17/1→17 in Figure 1c. An earlier SSNMR study attempted to test this hypothesis using samples each containing an equimolar mixture of two labeled HFPs, one with three sequential backbone ^{13}CO labels and the other with three sequential backbone ^{15}N labels (*27*). Detection of an average d_{CN} of >10 Hz for a G5-L7 ^{13}CO/G5-L7 ^{15}N sample and an F11-G13 ^{13}CO/F11-G13 ^{15}N sample was consistent with a fraction of in-register parallel HFP molecules. However, because the samples were extensively labeled, the data were also consistent with other parallel or antiparallel registries. In addition, the data reflected an average of many intermolecular d_{CN} values so it was not possible to determine the fraction of molecules with a particular registry. There have also been efforts to detect in-register parallel structure using SSNMR measurement of intermolecular

$^{13}C-^{13}C$ dipolar couplings (d_{CC}) where $d_{CC} = 7710/r_{CC}^3$, with d_{CC} in hertz and r_{CC} in angstroms. For HFP with a single ^{13}CO label and in-register parallel structure, the labeled interstrand $r_{CC} \approx 5$ Å and $d_{CC} \approx 70$ Hz (*28*, *29*). These parameters will be independent of the residue that is ^{13}CO-labeled. For membrane-associated HFP with F8 ^{13}CO, a best-fit d_{CC} of ≈70 Hz was detected, whereas for membrane-associated HFPtr, d_{CC} depended on the position of the labeled ^{13}CO residue with a range of 10−60 Hz (*30*, *31*). This residue dependence argued against a major fraction of in-register parallel structure in HFPtr.

There was also an IR spectroscopy effort to distinguish between the 1→17/1→17 parallel and 16→1/1→16 antiparallel registries using samples that contained backbone ^{13}CO labeling at either (1) A1 to V3 and G5 to I9, (2) F8 to G16, or (3) A1 to V3 and G5 to G16 (*32*). The IR wavenumbers and intensities of different samples were interpreted to support a large fraction of parallel structure and little antiparallel structure. However, in our view, the extensive labeling of the IR samples precluded quantitation of specific registries, and stronger support for this argument is provided in Discussion.

This paper reports a determination of the fraction of parallel structure in membrane-associated HFP oligomers. We were motivated to study this question because of (1) the functional significance of HIV fusion peptide oligomers and (2) the existing undefinitive and conflicting data and interpretations relevant to this question. As part of this effort, we developed a model to quantify the effects of natural abundance ^{13}C and ^{15}N nuclei on SSNMR measurements of d_{CN} and experimentally validated this model.

MATERIALS AND METHODS

Materials. 9-Fluorenylmethoxycarbonyl (FMOC)-protected amino acids and FMOC-Ala-Wang resin were purchased from Peptides International (Louisville, KY). Isotopically labeled amino acids were purchased from Cambridge Isotopes (Andover, MA) and were FMOC-protected using literature methods (*33*). Figure 1a shows the labeled HFPs. The 23 N-terminal residues (AVGIGALFLGFLGAAGSTMGARS) are a consensus sequence of the gp41 fusion peptide; non-native W24 is an A_{280} chromophore, and the non-native lysines greatly reduced the level of HFP aggregation in aqueous solution prior to membrane binding (*12*, *18*). This ensured that membrane-associated β sheet oligomers/aggregates were formed after membrane binding.

HFP was manually synthesized and then cleaved from the resin for 3 h in a solution of trifluoroacetic acid (TFA), water, anisole, thioanisole, and ethanedithiol in a 90:5:2:2:2 volume ratio. After precipitation with cold diethyl ether, centrifugation, and dissolution of the pellet in water, crude HFP was purified by reversed-phase high-performance liquid chromatography with a semipreparative C_4 column and a water/acetonitrile gradient containing 0.1% TFA. Acetonitrile and TFA were removed with nitrogen gas, and water was then removed by lyophilization. HFP purity was >95% as determined by mass spectrometry. HFP amounts were quantified using A_{280} of aqueous solutions of HFP with an ε of 5600 M^{-1} cm^{-1}.

SSNMR Samples. As shown in Figure 1b, each sample contained a ^{13}CO-labeled peptide and a ^{15}N-labeled peptide in a 1:2 molar ratio. Three samples contained membrane-associated HFP β sheet oligomers/aggregates that were each a statistical mixture of ^{13}CO- and ^{15}N-labeled HFPs. Detection of substantial d_{CN} by SSNMR indicated proximity of the labeled ^{13}CO and ^{15}N nuclei on adjacent strands and was used to estimate the fractional populations of specific registries as detailed below. As shown in Figure 1c, the HFP-P sample was designed to detect parallel 1→17/1→17 and 2→17/1→16 registries, the HFP-A sample was designed to detect previously observed antiparallel 16→1/1→16 and 17→1/1→17 registries, and the HFP-AP sample was designed to detect both parallel 1→17/1→17 and 2→17/1→16 registries and antiparallel 16→1/1→16 and 17→1/1→17 registries.

In addition to the potential proximity of labeled ^{13}CO and ^{15}N nuclei, there will always be proximity between labeled ^{13}CO and some natural abundance (na) ^{15}N nuclei as well as proximity between some na ^{13}CO and labeled ^{15}N nuclei. These proximities will contribute to the d_{CN} detected in the SSNMR experiment and should be included in the data modeling. Quantitative understanding of these proximities required a negative control (HFP-NC) sample with (1) the same relative fractions of labeled ^{13}CO, ^{15}N, and na sites as the HFP-P, HFP-A, and HFP-AP samples and (2) labeled ^{13}CO−labeled ^{15}N r_{CN} values that are much greater than the REDOR detection limit of ∼7 Å. One possibility was a sample made like HFP-P, HFP-A, and HFP-AP but with labels at sites that do not form intermolecular hydrogen bonds. This possibility was not pursued because the distribution of registries of membrane-associated HFP is not yet well-defined. Instead, the HFP-NC sample was a physical mixture of lyophilized HFP-F8 (5.0 mg) and HFP-A6L7 (10.0 mg) without any membrane. Each peptide was lyophilized separately, and the two peptides were then mixed in the solid phase to form a uniform physical mixture. Water and membrane were not added to the physical mixture so that the labeled ^{13}CO and ^{15}N groups remained much farther apart than the 7 Å REDOR detection limit. Although there were populations of β sheet as well as α helical lyophilized peptides in the HFP-NC sample, each population yielded a very similar $\Delta S/S_0$ value (see Results for further details).

For the HFP-P, HFP-A, and HFP-AP samples, the membrane consisted of 1,2-di-*O*-tetradecyl-*sn*-glycero-3-phosphocholine (DTPC) lipid, 1,2-di-*O*-tetradecyl-*sn*-glycero-3-[phospho-*rac*-(1-glycerol)] (DTPG) lipid, and cholesterol in an 8:2:5 molar ratio. This composition reflected the large amount of choline lipid and fractions of negatively charged lipid and cholesterol in membranes of host cells of HIV (*16*). Ether-linked rather than more physiologically abundant ester-linked lipids were used because the latter have two COs per molecule that would contribute substantial na ^{13}CO signal. The bilayer phase is retained for ether-linked lipids with cholesterol and with HFP (*34*−*36*). In addition, membrane-associated HFP has predominant β sheet structure in either ester-linked lipid with cholesterol or ether-linked lipid with cholesterol (*30*).

We prepared samples by first dissolving DTPC (40 μmol), DTPG (10 μmol), and cholesterol (25 μmol) in chloroform and removing the chloroform with nitrogen gas and vacuum. The lipid film was suspended in 2 mL of 5 mM HEPES buffer (pH 7.0) with 0.01% NaN_3 preservative. The suspension was homogenized with 10 freeze−thaw cycles, and large unilamellar vesicles were formed by extrusion through a 100 nm diameter polycarbonate filter (Avestin, Ottawa, ON). A separate solution was prepared with ^{13}CO-labeled HFP (3.0 mg) and ^{15}N-labeled HFP (6.0 mg) in HEPES buffer (32 mL). The HFP solution was added dropwise to the vesicle solution, and the combined solution was gently stirred overnight. Ultracentrifugation at ∼150000*g* for 4 h pelleted membranes with bound HFP while unbound HFP remained in the supernatant (*14*). The pellet was lyophilized, transferred to the SSNMR rotor, and rehydrated with 30 μL of H_2O (*37*). The validity of the lyophilization−rehydration approach

was evidenced by peak ^{13}CO chemical shifts that were within 0.6 ppm of those of samples that were not lyophilized (*15*).

SSNMR Experiments. Data were collected on a 9.4 T spectrometer (Varian Infinity Plus, Palo Alto, CA) using a triple-resonance MAS probe equipped for 4.0 mm rotors and tuned to ^{13}C, ^{1}H, and ^{15}N nuclei at frequencies of 100.8, 400.8, and 40.6 MHz, respectively. The ^{13}C chemical shift was externally referenced to the methylene resonance of adamantane at 40.5 ppm, and the ^{13}C transmitter was set to 153 ppm. The ^{13}CO−^{15}N dipolar coupling (d_{CN}) was probed with the rotational-echo double-resonance (REDOR) experiment with typical parameters: (1) 52 kHz ^{1}H $\pi/2$ pulse, (2) 2.2 ms cross polarization with a 74 kHz ^{1}H field and a 83−98 kHz ramped ^{13}C field, (3) dephasing period of duration τ for which the "S_0" and "S_1" acquisitions had 60 kHz ^{13}C π pulses at the end of each rotor cycle except the last cycle and the S_1 acquisitions additionally had 59 kHz ^{15}N π pulses in the middle of each rotor cycle, and (4) ^{13}C detection (*30*, *38*). The MAS frequency was 10 kHz and the recycle delay 2 s; 88 kHz TPPM ^{1}H decoupling was applied during the dephasing and detection periods, and XY-8 phase cycling was applied to the ^{13}C π pulses and to the ^{15}N π pulses (*39*, *40*). Experiments were calibrated using a lyophilized helical peptide with an AEAAAKEAAAKEAAAKA sequence, N-terminal acetylation and C-terminal amidation, and A9 ^{13}CO and A13 ^{15}N labels (*30*, *41*). The labeled r_{CN} of ≈4.1 Å corresponds to a d_{CN} of ≈45 Hz. Samples were typically cooled with nitrogen gas at −50 °C to enhance the ^{13}CO signal and reduce motional averaging of d_{CN} (*42*). The typical difference between the ^{13}C shift in cooled and uncooled membrane-associated HFP samples is ≤0.5 ppm and indicates little variation in secondary structure with temperature (*26*). For each sample, data were collected for τ values of 2.2, 8.2, 16.2, 24.2, 32.2, 40.2, and 48.2 ms.

The ^{13}CO−^{15}N dipolar coupling, d_{CN}, is detected by reduction of the ^{13}CO signal intensity in the S_1 spectrum relative to the S_0 spectrum with greater reduction at increased τ values. These intensities were also denoted S_1 and S_0 and were determined from integration over a shift range that encompassed most of the ^{13}CO signal. A range of 8 ppm was used for HFP-NC spectra and a range of 5 ppm for HFP-P, HFP-A, and HFP-AP spectra. The normalized dephasing

$$\left(\frac{\Delta S}{S_0}\right)^{\exp} = \frac{{S_0}^{\exp} - {S_1}^{\exp}}{{S_0}^{\exp}} = 1 - \frac{{S_1}^{\exp}}{{S_0}^{\exp}} \quad (1)$$

and its standard deviation

$$\sigma^{\exp} = \sqrt{\frac{{S_0}^2{\sigma_{S_0}}^2 + {S_1}^2{\sigma_{S_1}}^2}{{S_0}^2}} \quad (2)$$

where σ_{S_0} and σ_{S_1} were the experimental root-mean-square deviations of the spectral intensities derived from 12 regions of the spectrum that did not include spectral features (*43*).

Experimental dephasing of a membrane-associated HFP sample was modeled as a sum of S_0 and a sum of S_1 signals of different spin geometries of ^{13}CO and ^{15}N nuclei where the geometries reflected statistical distributions of na ^{13}CO and ^{15}N nuclei as well as geometries of (1) 1→17/1→17 and 2→17/1→16 parallel adjacent strand registries, (2) 16→1/1→16 and 17→1/1→17 antiparallel registries, and (3) other "X" registries where all labeled r_{CN} values were > 7 Å and $S_1 = S_0$. The notation $(\Delta S/S_0)^{sim}$ will be generally used for simulated $\Delta S/S_0$ and can refer to a particular spin geometry or to the population-weighted sum using calculations from different spin geometries. For the former case, the $(S_1/S_0)^{sim} \equiv \gamma$ values were calculated using the SIMPSON program with input parameters that included d_{CN} values as well as Euler angles in a fixed crystal frame for each ^{13}CO−^{15}N vector and for the ^{13}CO chemical shift anisotropy (CSA) principal axis system (*44*, *45*). These input parameters were calculated with SIMMOL using ^{13}CO and ^{15}N coordinates from a region of a high-resolution crystal structure with the appropriate structural motif, e.g., parallel β sheet (*46*). Coordinates were obtained from the following Protein Data Bank (PDB) entries: 1JK3, 1IGD, 1NKI, 2E4T, 1CEX, 1MNZ, and 2IWW. For each spin geometry, $(S_1/S_0)^{sim}$ was the average of 10 different SIMPSON calculations, and each calculation was based on input parameters from a different set of atomic coordinates. The ^{13}CO CSA principal values of 247, 176, and 99 ppm were inputs to the SIMPSON calculations, and ^{1}Hs and relaxation were not considered.

RESULTS

Chemical Shift and Conformational Distributions. Figure 2 displays REDOR S_0 and S_1 ^{13}C SSNMR spectra for a τ of 32.2 ms. Each S_0 spectrum has an ∼50% contribution from the labeled ^{13}CO and ∼50% contribution from na ^{13}COs of the unlabeled residues. The full width at half-maximum line widths of the membrane-associated HFP samples in Figure 2b−d are 3−4 ppm and indicate a distinct secondary structure. For the HFP-AP sample with the F8 ^{13}CO label, the peak ^{13}CO shift of 173 ppm is the same as that observed for F8 ^{13}CO of HFP in a known β strand conformation and is very different from the 178 ppm shift observed in the α helical conformation (*15*, *30*). For the HFP-P and HFP-A samples with the L12 ^{13}CO label, the 174 ppm peak shift is also the same as that of β strand HFP and different from the 179 ppm shift of Leu in helical HFP (*30*, *47*). Overall, the shifts and line widths are consistent with the fully extended conformation that has been observed for the first 16 residues of HFP associated with membranes with biologically relevant cholesterol content (*15*).

The line width of the lyophilized HFP-NC sample with an F8 ^{13}CO label is ∼7 ppm and correlates with a broad distribution of secondary structures that is also evidenced by a 176 ppm peak ^{13}CO shift that is midway between typical Phe helical and β strand shifts (*48*).

Qualitative Analysis of REDOR Data. Relative to the S_0 signals, there is attenuation in the S_1 signals of ^{13}COs within ∼7 Å of ^{15}Ns and the associated $\Delta S/S_0$-normalized dephasing increased with dephasing time (Figures 2 and 3). Because of the physical separation of the ^{13}CO- and ^{15}N-labeled HFPs in HFP-NC, the S_1 attenuation and $(\Delta S/S_0)^{exp}$ of this sample reflected F8 ^{13}CO−na ^{15}N and na ^{13}CO−A6,L7 ^{15}N proximities but not F8 ^{13}CO−A6, L7 ^{15}N proximity (Figures 2a and 3a). There was similar S_1 attenuation and $(\Delta S/S_0)^{exp}$ in HFP-P (Figures 2b and 3b), which demonstrated that there was little L12 ^{13}CO−G13,A14 ^{15}N proximity in HFP-P and only a small fraction of parallel 1→17/1→17 and 2→17/1→16 registries. There was much more S_1 attenuation and a larger $(\Delta S/S_0)^{exp}$ for the HFP-A sample (Figures 2c and 3b), which indicated significant L12 ^{13}CO−G5,A6 ^{15}N proximity and therefore a substantial fraction of antiparallel 16→1/1→16 and 17→17/1→17 registries. Comparably strong S_1 attenuation and a large $(\Delta S/S_0)^{exp}$ were observed for the HFP-AP sample (Figures 2d and 3b). The similarity of the HFP-NC and HFP-P data and the similarity of the HFP-A and HFP-AP data were consistent with ascribing F8 ^{13}CO−L9,G10 ^{15}N proximity in HFP-AP to antiparallel 16→1/1→16 and 17→1/1→17 registries

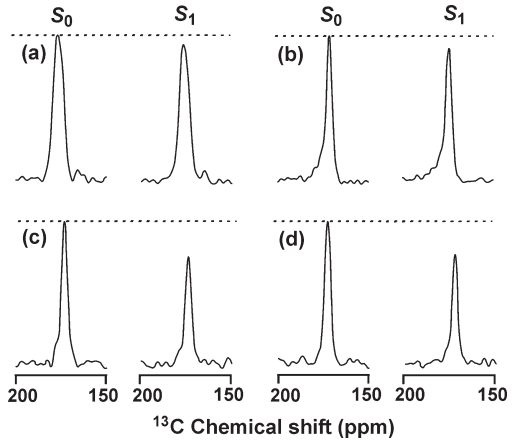

FIGURE 2: REDOR S_0 and S_1 ^{13}C SSNMR spectra with a 32.2 ms dephasing time for (a) HFP-NC, (b) HFP-P, (c) HFP-A, or (d) HFP-AP. Each spectrum was processed with 200 Hz line broadening and baseline correction and was the sum of (a) 38624, (b) 23488, (c) 24914, or (d) 14240 scans. Relatively narrow ^{13}CO signals were observed in the HFP-P, HFP-A, and HFP-AP samples because the HFPs were membrane-associated with predominant β sheet conformation at the labeled ^{13}CO site. A broader ^{13}CO signal was observed in the HFP-NC sample because there was no membrane and there were populations of lyophilized HFP with either α helical or β sheet conformation at the labeled ^{13}CO site.

rather than parallel 1→17/1→17 and 2→17/1→16 registries. Detection of a substantial fraction of these antiparallel registries is consistent with earlier SSNMR data for sparsely labeled HFP (*15*). Detection of only a small fraction of parallel registries is a new result and disagrees with previous interpretations of SSNMR and IR data for samples with extensive labeling (*27*, *32*). These new data highlight the importance of sparse labeling in reducing interpretational ambiguity for systems with a structural distribution like membrane-associated HFP.

Natural Abundance Models. Quantitative analysis of the $(\Delta S/S_0)^{exp}$ to yield the fraction of parallel and antiparallel HFP registries requires an accurate natural abundance dephasing (nad) model, i.e., a model that accounts for effects of labeled ^{13}CO−na ^{15}N and na ^{13}CO−labeled ^{15}N proximities. Both types of proximities were considered, but for the sake of conciseness, the discussion in this paper focuses on labeled ^{13}CO−na ^{15}N proximity. One measure of validity of a nad model was agreement within experimental error between $(\Delta S/S_0)^{exp}$ of HFP-NC and $(\Delta S/S_0)^{sim}$ of the model. Consideration was first given to the HFP-F8 regions of HFP-NC, including the spin geometries of one or two labeled ^{13}COs and one na ^{15}N. Geometries with two or more na ^{15}Ns were not considered because the fractional isotopic abundance of ^{15}N is only 0.0037. For each geometry, SIMPSON was used to calculate $(S_1/S_0)^{sim}$ as a function of dephasing time τ. Only geometries with r_{CN} values of < 7 Å were considered because those with r_{CN} values of > 7 Å do not affect $(S_1/S_0)^{sim}$ within our experimental signal-to-noise range. We consider this a "long-range" nad model that is distinguished from a "short-range" model of earlier studies that only considered na nuclei separated by one or two bonds from a labeled nucleus, i.e., $r_{CN} < 3$ Å (*15*, *30*). The broad spectral line width of HFP-NC indicated both helical and β strand conformational populations, and coordinates of spin geometries for both α helical and β sheet structures were obtained from corresponding regions of high-resolution structure PDB entries. For α helical structure, the $r_{CN} < 7$ Å criterion resulted in geometries with a single labeled ^{13}CO at residue i and a single na ^{15}N at a residue between positions

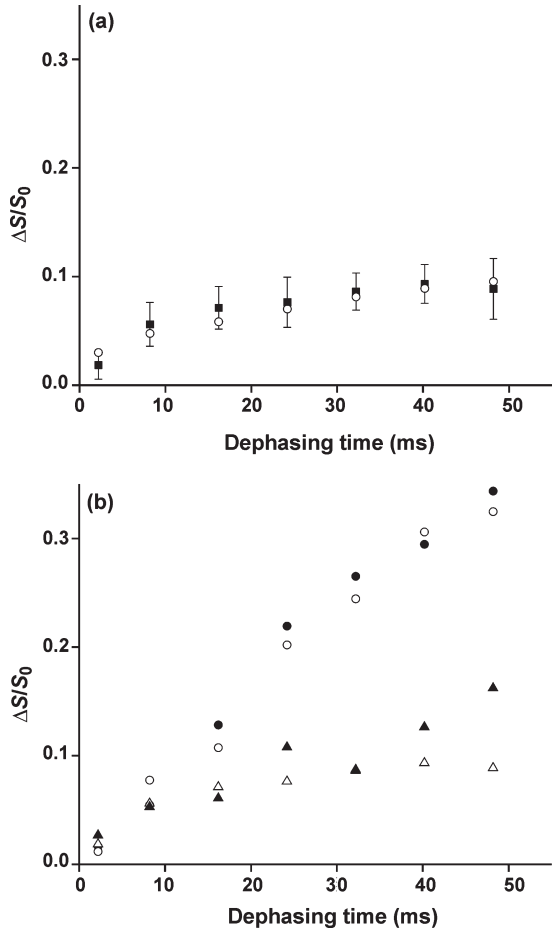

FIGURE 3: (a) Plot of REDOR $(\Delta S/S_0)^{exp}$ (■) and $(\Delta S/S_0)^{sim}$ (○) vs dephasing time for the lyophilized HFP-NC sample. The $(\Delta S/S_0)^{sim}$ values were calculated using a mixture of nad models with fractional populations: α helical, 0.5; minimal β sheet, 0.25; maximal β sheet, 0.25. (b) Plots of $(\Delta S/S_0)^{exp}$ vs dephasing time for HFP-NC (△), HFP-P (▲), HFP-A (○), and HFP-AP (●). The typical σ^{exp} is ±0.02. A variation of ±0.02 in $(\Delta S/S_0)^{exp}$ was also observed between two different preparations of the same sample type, e.g., HFP-A.

$i - 3$ and $i + 5$. These nine geometries make up one aspect of the α nad model.

Figure 4 illustrates relevant labeled ^{13}COs and na ^{15}Ns for antiparallel β sheet structure. The strands in panels a and c are "fully constrained" to a single registry with six resultant unique spin geometries. Three geometries had one labeled ^{13}CO and one na ^{15}N within the same strand, and three geometries had two labeled ^{13}COs on vicinal strands and one na ^{15}N in the intervening strand. In panels b and d, the strands have different registries so that the labeled ^{13}CO in the top strand was > 7 Å from the nine na ^{15}N sites of the ^{13}CO of the third strand. The structure of panels b and d has nine unique spin geometries and is denoted a maximum β sheet nad (max β nad) model, while the structure of panels a and c has six geometries and is denoted a minimum β sheet nad (min β nad) model. In both structures, there are nine na ^{15}N sites within 7 Å of each labeled ^{13}CO, but in the min nad model, some sites (e.g., 4−6 in Figure 4c) are "shared" between two ^{13}COs, i.e., within 7 Å of two ^{13}COs. This reduces the average number of na ^{15}N sites per ^{13}CO and the overall nad.

There are many indices and parameters in the quantitative modeling, and descriptions and possible values for them are

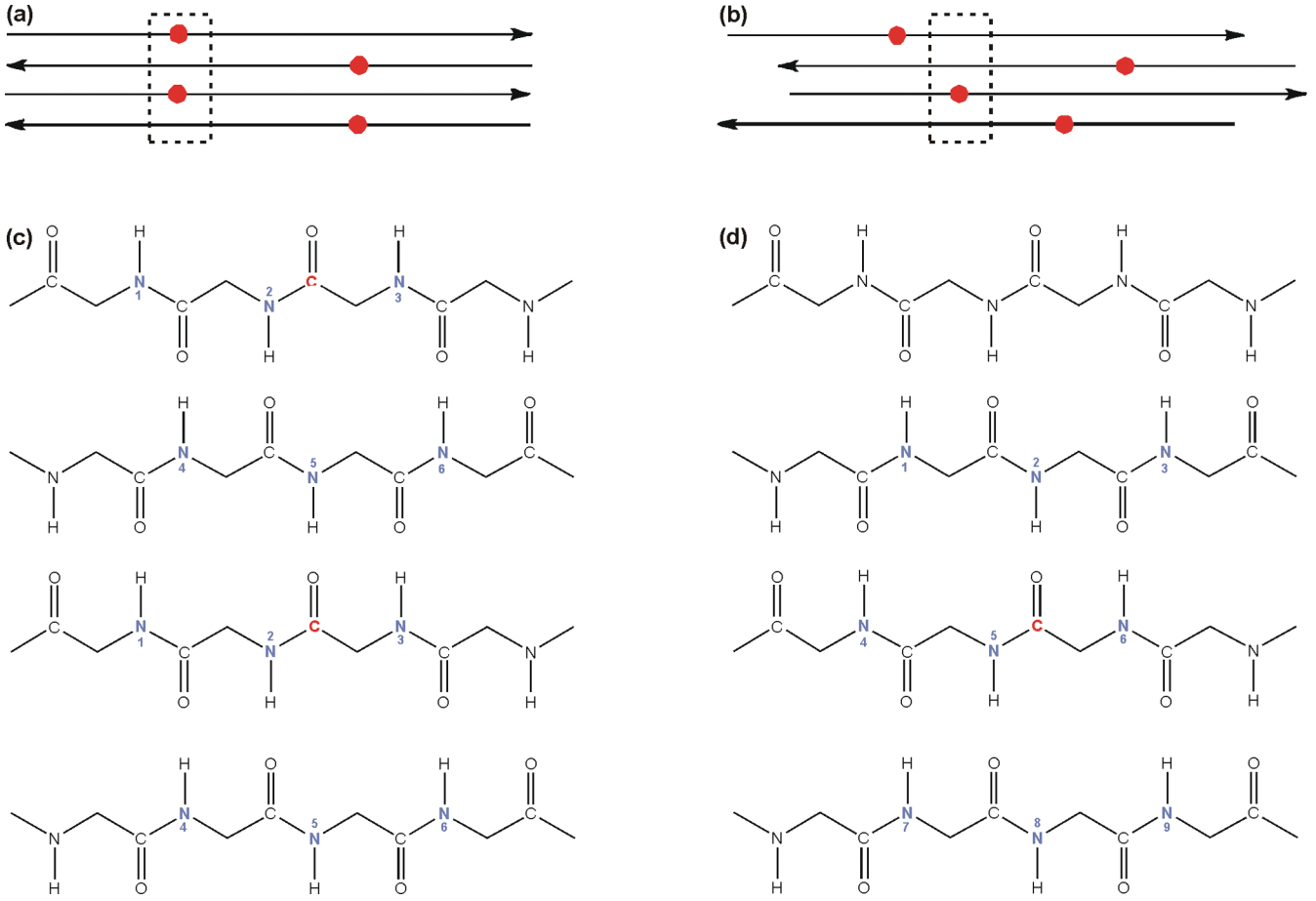

FIGURE 4: (a and b) Schematic diagrams of the HFP-F8 region of the HFP-NC sample in antiparallel β sheet structure with labeled ^{13}COs represented as red circles. Panel a shows a model that is fully constrained to a single registry, while panel b shows multiple registries. (c and d) β sheet backbone representations of the respective boxed regions of panels a and b with labeled ^{13}COs colored red and possible na ^{15}N sites colored blue, i.e., sites for which a na ^{15}N is within 7 Å of a labeled ^{13}CO. A particular spin geometry will have only one ^{15}N. The min nad model is shown in panel c, and each spin geometry will have either one labeled ^{13}CO and one na ^{15}N (1, 2, or 3) or two labeled ^{13}COs and one na ^{15}N (4, 5, or 6). The max nad model is shown in panel d, and each spin geometry will have one labeled ^{13}CO and one na ^{15}N.

compiled in Table 1. For the α, min β, or max β nad models, the average $\gamma = S_1/S_0$ for the relevant spin geometries:

$$\gamma_{lN}^{\mathrm{na}}(\tau) = J^{-1}\sum_{j=1}^{J}\left[\frac{S_{lj}(\tau)}{S_{0j}(\tau)}\right]^{\mathrm{sim}} \quad (3)$$

where na refers to natural abundance, $l = 0$ or 1, N refers to na ^{15}N, j is the index of a particular spin geometry, and J is the number of unique spin geometries of the model ($J = 9$ for α or max β nad, and $J = 6$ for min β nad). The $\gamma_{0N}^{\mathrm{na}}(\tau) = 1$ for all values of τ, while $\gamma_{1N}^{\mathrm{na}}(\tau)$ values were calculated using $[S_{1j}(\tau)/S_{0j}(\tau)]^{\mathrm{sim}}$ from SIMPSON and generally decreased with increasing τ values. After a total labeled ^{13}CO population of 1.0 for HFP-F8 in HFP-NC has been set, the relative population affected by na ^{15}N is $J \times 0.0037$ while the remainder population, $1 - (J \times 0.0037)$, has $S_1 = S_0$. There is also an na ^{13}CO contribution from unlabeled residues in HFP-F8 with a relative population of 30×0.011 and with $S_1 = S_0$. Similar analysis for ^{15}N-labeled HFP-A6L7 in HFP-NC results in

$$\gamma_{lC}^{\mathrm{na}}(\tau) = K^{-1}\sum_{k=1}^{K}\left[\frac{S_{lk}(\tau)}{S_{0k}(\tau)}\right]^{\mathrm{sim}} \quad (4)$$

where $l = 0$ or 1, C refers to na ^{13}CO, k is the index of a particular spin geometry, K is the number of unique na ^{13}CO-labeled ^{15}N spin geometries of the model ($K = 10$, 8, or 12 for α, min β, or max β nad models, respectively), and $\gamma_{0C}^{\mathrm{na}}(\tau) = 1$. If we account for the 1:2 HFP-F8:HFP-A6L7 ratio, the total na ^{13}CO population of HFP-A6L7 is $2 \times 31 \times 0.011$ with population $2K \times 0.011$ affected by labeled ^{15}N and the remainder having $S_1 = S_0$. For HFP-NC in total

$$S_{l,\mathrm{tot}}^{\mathrm{sim}}(\tau) = [J \times 0.0037 \times \gamma_{lN}^{\mathrm{na}}(\tau)] + [2K \times 0.011 \times \gamma_{lC}^{\mathrm{na}}(\tau)] + (2.0 - J \times 0.0037 - 2K \times 0.011) \quad (5)$$

where $l = 0$ or 1 and the terms in the first two sets of brackets are τ- and l-dependent.

For each nad model (α, min β, and max β), the $(\Delta S/S_0)^{\mathrm{sim}}$ for each τ was calculated with eq 5 and statistical comparison was then made to $(\Delta S/S_0)^{\mathrm{exp}}$:

$$\chi^2 = \sum_{m=1}^{7}\left[\frac{\left(\frac{\Delta S}{S_0}\right)_m^{\mathrm{sim}} - \left(\frac{\Delta S}{S_0}\right)_m^{\mathrm{exp}}}{\sigma_m^{\mathrm{exp}}}\right]^2 \quad (6)$$

where m is the index for an experimental datum, i.e., a particular τ. The χ^2 values for the α, min β, and max β nad models were 1.2, 3.8, and 2.0, respectively, which were all less than the number of degrees of fitting, 7, i.e., the number of data, 7, minus the number

Table 1: Indices and Parameters

index or parameter	description	values
f_t	fractional population of structure t	for membrane-associated samples, determined by fitting
j, k	index for na site <7 Å from a labeled site: j, na ^{15}N near labeled ^{13}CO; k, na ^{13}CO near labeled ^{15}N	
J, K	number of na sites <7 Å from a labeled site: J, na ^{15}Ns near labeled ^{13}CO; K, na ^{13}COs near labeled ^{15}N	α helical structure, $J = 9$ and $K = 10$; min β sheet structure, $J = 6$ and $K = 8$; max β sheet structure, $J = 9$ and $K = 12$
l	REDOR data type index	$0 \equiv$ no dipolar evolution $1 \equiv$ dipolar evolution
m	datum index	1, 2, 3, 4, 5, 6, or 7
S_l, S_{lj}, S_{lk}, S_{lu}	REDOR signal intensity	determined by experiment or calculation
t, t_1, t_2	structural population index; for an unconstrained model of membrane-associated samples, t_1 indexes the top/middle registry and t_2 indexes the middle/bottom registry	for membrane-associated samples: $1 \equiv$ parallel registry, $2 \equiv$ antiparallel registry, $3 \equiv$ other "X" registry
u	membrane-associated sample index	$1 \equiv$ HFP-P, $2 \equiv$ HFP-A, $3 \equiv$ HFP-AP
v	index for arrangement of three adjacent labeled HFPs in membrane-associated samples; middle HFP has ^{13}CO labeling, and the ^{13}CO is hydrogen bonded to HN of the top HFP	$1 \equiv$ ^{13}CO HFP (top), ^{13}CO HFP (bottom) $2 \equiv$ ^{15}N HFP (top), ^{13}CO HFP (bottom) $3 \equiv$ ^{13}CO HFP (top), ^{15}N HFP (bottom) $4 \equiv$ ^{15}N HFP (top),^{15}N HFP (bottom)
w_v	fractional population of arrangement of three adjacent labeled HFPs in membrane-associated samples	fully constrained model: $w_1 = 1/9$, $w_2 = 2/9$, $w_3 = 2/9$, $w_4 = 4/9$; unconstrained model: $w_1 = 1/81$, $w_2 = 2/81$, $w_3 = 2/81$, $w_4 = 4/81$
$\gamma_{lN}^{na}(\tau)$, $\gamma_{lC}^{na}(\tau)$	$S_l(\tau)/S_0$: $\gamma_{lN}(\tau)$, labeled ^{13}CO−na ^{15}N proximity; $\gamma_{lC}(\tau)$, na ^{13}CO−labeled ^{15}N proximity	$\gamma_{0N}(\tau) = 1$, $\gamma_{0C}(\tau) = 1$, $\gamma_{1N}(\tau)$ and $\gamma_{1C}(\tau)$ determined by calculation
$\gamma_{ltuv}^{lab}(\tau)$, $\gamma_{lt_1t_2uv}{}^{lab}(\tau)$	$S_{lu}^{lab}(\tau)/S_0{}^{lab}$ for arrangement of labeled ^{13}CO and ^{15}N nuclei: $\gamma_{1tuv}^{lab}(\tau)$, fully constrained model; $\gamma_{1t_1t_2uv}{}^{lab}(\tau)$, unconstrained model	$\gamma_{0tuv}^{lab}(\tau) = 1$, $\gamma_{0t_1t_2uv}{}^{lab}(\tau) = 1$, $\gamma_{1tuv}^{lab}(\tau)$ and $\gamma_{1t_1t_2uv}{}^{lab}(\tau)$ determined by calculation
τ	REDOR dephasing time	2.2, 8.2, 16.2, 24.2, 32.2, 40.2, or 48.2 ms

of independent fitting parameters, 0. The validity of the approach to nad calculation was supported by good fits for all models (*43*).

The broad ^{13}CO line width of HFP-NC in Figure 2a was consistent with two HFP populations, one with helical and one with β strand secondary structure. It was therefore reasonable to calculate $(\Delta S/S_0)^{sim}$ for "mixtures" with contributions from multiple models:

$$S_{l,\,mix}^{sim}(\tau) = \sum_{t=1}^{3} f_t S_{lt}^{sim}(\tau)] \qquad (7)$$

where $l = 0$ or 1, t was the index that referred to the α, min β, or max β model, f_t was the fractional population with $\Sigma f_t = 1$, and each $S_{lt}^{sim}(\tau)$ was calculated using eq 5. The HFP-NC distribution of ^{13}CO shifts indicated $f_\alpha \approx 0.5$ and $f_{min\beta} + f_{max\beta} \approx 0.5$ but did not provide information about individual $f_{min\beta}$ or $f_{max\beta}$. Fitting using an f_α of 0.5, an $f_{min\beta}$ of 0.5, and an $f_{max\beta}$ of 0.0 yielded a χ^2 of 1.5, while fitting using either an f_α of 0.5, an $f_{min\beta}$ of 0.0, and an $f_{max\beta}$ of 0.5 or an f_α of 0.5, an $f_{min\beta}$ of 0.25, and an $f_{max\beta}$ of 0.25 yielded a χ^2 of 1.2. $(\Delta S/S_0)^{sim}$ values in Figure 3a were calculated with the latter distribution. The $(\Delta S/S_0)^{sim}$ values from all three conformational distributions fit well to the $(\Delta S/S_0)^{exp}$, and these models are statistically similar. Together with previously described good fitting for different secondary structure models show that nad is accurately calculated with these models and only weakly dependent on secondary and tertiary structure. The key feature of all these well-fitting long-range models was consideration of the multiple na sites within 7 Å of a labeled site, which led to continually increasing $\Delta S/S_0$ with τ (Figure 3a). The $(\Delta S/S_0)^{sim}$ values were also calculated using a short-range model that considered only na sites separated by one or two bonds from each labeled site. The $(\Delta S/S_0)^{sim}$ values were systematically lower than the $(\Delta S/S_0)^{exp}$ values with the resultant poor fit, and $\chi^2 = 29$.

Quantitative Analysis of Registry Populations in the Fully Constrained Model. For membrane-associated HFP, there is a single distribution of registries that we model as fractions of (1) 1→17/1→17 and 2→17/1→16 parallel registries, (2) 16→1/1→16 and 17→1/1→17 antiparallel registries, and (3) X registries not detected by any of our labeling schemes (Figure 1c). Fraction 1 contributed to the $(\Delta S/S_0)^{exp}$ of HFP-P, fraction 2 to the $(\Delta S/S_0)^{exp}$ of HFP-A, and fractions 1 and 2 to the $(\Delta S/S_0)^{exp}$ of HFP-AP. The overall goal was best-fit determination of these fractions based on the $(\Delta S/S_0)^{exp}$ of the three samples (Figure 3b), and this analysis required calculation of the nad contribution to $(\Delta S/S_0)^{exp}$. Because a 1:2 ^{13}CO-HFP:^{15}N-HFP ratio was used for all samples, this contribution was calculated using models developed for HFP-NC and resulted in a modified eq 5 appropriate for HFP-P, HFP-A, and HFP-AP:

$$S_{lu,\,tot}^{sim}(\tau) = \{[J \times 0.0037 \times \gamma_{ln}^{na}(\tau)] + [2K \times 0.011 \times \gamma_{lC}^{na}(\tau)]\} + \{1.0 - 2K \times 0.011\} + (1.0 - J \times 0.0037)\gamma_{ltuv}^{lab}(\tau) \qquad (8)$$

$$= S_l^{na}(\tau) + S_{lu}^{lab}(\tau) \qquad (9)$$

where S_l^{na} is the sum of the first two terms in braces in eq 8 and S_{lu}^{lab} is the third term. Each membrane-associated sample is labeled by the index u where $u = 1$, 2, or 3, which refers to HFP-P, HFP-A, or HFP-AP, respectively (Table 1 and Figure 1b). The first braced term in eq 8 corresponds to labeled and na ^{13}CO that experience nad; the second braced term corresponds to na ^{13}COs that do not experience nad, and the third term corresponds to labeled ^{13}COs that do not experience nad but may experience dephasing from labeled ^{15}Ns. The secondary structure of membrane-associated HFP was predominantly β sheet (Figure 2b−d), and the best estimates of the nad terms in the first braced term were taken to be

the average of the max β and min β calculated values. In the second and third braced terms, K and J were estimated to be their average values of 10 and 7.5, respectively. $S_{0u}^{lab}(\tau)$ was calculated using a $\gamma_{0tuv}^{lab}(\tau)$ of 1, while $\gamma_{1tuv}^{lab}(\tau)$ and therefore $S_{1u}^{lab}(\tau)$ were first calculated with a "fully constrained" model (Figure 4a,c) in which a β sheet region contained either (1) 1→17/1→17 or 2→17/1→16 parallel registries, (2) 16→1/16→1 or 17→1/1→17 antiparallel registries, or (3) X registries not directly detected by any of our labeling schemes (Figure 1c). A sample was considered to be a mixture of the three registry types each denoted by index $t = 1$, 2, or 3 and fractional population f_t (Table 1). $S_{1u}^{lab}(\tau)$ was calculated by modified eq 7:

$$S_{1u}^{lab}(\tau) = \sum_{t=1}^{3} [f_t \gamma_{1tuv}^{lab}(\tau)] \times S_0^{lab}(\tau) \quad (10)$$

The $\gamma_{1tuv}^{lab}(\tau)$ values depended on the labeled d_{CN} values and therefore r_{CN} values, which in turn depended on registry type t and sample labeling u (Figure 1c). For some combinations of t and u, all labeled r_{CN} values are > 7 Å with consequent $d_{CN} \approx 0$ and $\gamma_{1tuv}^{lab}(\tau) = 1$. Specific examples are $t = 1$ and $u = 2$, $t = 2$ and $u = 1$, and $t = 3$ and $u = 1$, 2, or 3. For other combinations of t and u, $\gamma_{1tuv}^{lab}(\tau)$ values were determined from SIMPSON calculations, and Figure 5a−d displays schematic examples for $t = 2$ and $u = 2$ with numerical values of $\gamma_{1tuv}^{lab}(\tau)$ in the Supporting Information. Column a, b, c, or d corresponds to particular arrangements of ^{13}CO- and ^{15}N-labeled HFPs that are denoted by the index $v = 1$, 2, 3, or 4, respectively. For each v, the typical difference between the calculated $\gamma_{122v}^{lab}(\tau)$ for the 16→1/1→16 or 17→1/1→17 registry was ≤0.01 and the final $\gamma_{122v}^{lab}(\tau)$ values were the average for the two registries. The antiparallel $\gamma_{123v}^{lab}(\tau)$ values of HFP-AP were analogously calculated, and the parallel $\gamma_{111v}^{lab}(\tau)$ values of HFP-P and parallel $\gamma_{113v}^{lab}(\tau)$ values of HFP-AP were calculated using the 1→17/1→17 registry and were similar to γ values calculated using the 2→17/1→16 registry. Fractional weightings w_v were based on the 1:2 ^{13}CO HFP:^{15}N HFP ratio with $w_1 = 1/9$, $w_2 = 2/9$, $w_3 = 2/9$, and $w_4 = 4/9$. A more complete version of eq 10

$$S_{1u}^{lab}(\tau) = \sum_{t=1}^{3} \left\{ f_t \times \sum_{v=1}^{4} \left[w_v \gamma_{1tuv}^{lab}(\tau) \right] \right\} \times S_0^{lab}(\tau) \quad (11)$$

with indices and parameters summarized in Table 1.

The values of f_1, f_2, and f_3 were the same for the HFP-P, HFP-A, and HFP-AP samples, where $f_3 = 1 - f_1 - f_2$. Best-fit values of f_1 and f_2 were obtained by calculating $\chi^2(f_1,f_2)$ using an expression analogous to eq 6:

$$\chi^2(f_1,f_2) = \sum_{u=1}^{3} \sum_{m=1}^{7} \left\{ \frac{\left[\frac{\Delta S(f_1,f_2)}{S_0} \right]_{um}^{sim} - \left(\frac{\Delta S}{S_0} \right)_{um}^{exp}}{\sigma_{um}^{exp}} \right\}^2 \quad (12)$$

and then selecting the f_1 and f_2 values that corresponded to the minimal χ^2, i.e., χ^2_{min}. In eq 12, m is the index for each τ and $[\Delta S(f_1,f_2)/S_0]_{um}^{sim}$ was determined using eqs 8−11. For this fully constrained model, Figure 6a displays a plot of χ^2 versus f_1 and f_2 with the following best-fit values: $f_1 = 0.12$, $f_2 = 0.52$, and $\chi^2_{min} = 11$. The model was reasonable as evidenced by the χ^2_{min} that was smaller than the number of degrees of fitting, 19, i.e., the number of data, 21, minus the number of fitting parameters, 2. The f_1 fractional parallel population (Figure 1c) was small, which was consistent with qualitative analysis of the data (Figure 3b). The f_2 antiparallel population was substantially larger and also consistent with Figure 3b. The f_3 of ≈0.35 indicated a substantial population of X registries not detected by the labeling of the three samples.

The fitting described above was done using a long-range nad model that considered effects of na sites within 7 Å of each labeled nucleus. The fitting displayed in Figure 6a was based on nad calculated from half-min β and half-max β sheet structure (Figure 4), but the best-fit f_1, f_2, and χ^2_{min} were not sensitive to the structural composition of the long-range nad model. For example, fitting done using nad for half-α helical and half-max β sheet structure yielded best-fit f_1, f_2, and χ^2_{min} values within 0.01, 0.01, and 1 unit, respectively, of the corresponding values in Figure 6a. For HFP-NC fitting, the nad model was underestimated by a short-range model that considered only na sites separated by one or two bonds from each labeled site. This effect was also observed when fitting membrane-associated HFP data with the short-range nad model and led to a best-fit f_1 of 0.22 and a best-fit f_2 of 0.57, which were significantly higher than the values in Figure 6a. The χ^2_{min} of 20 using the short-range model was also higher than the χ^2_{min} in Figure 6a.

Quantitative Analysis of Registry Populations in the Unconstrained Model. In addition to the fully constrained model for strand registries, an alternate "unconstrained" fitting model was also considered for which there was local mixing of (1) 1→17/1→17 parallel registries, (2) 16→1/1→16 and 17→1/1→17 antiparallel registries, an (3) X registries not directly detected by any of our labeling schemes (Figure 1c). Each pairwise registry type was labeled by $t = 1$, 2, or 3 with fractional population f_t. For this unconstrained model, Figure 5e−h displays schematics of three-strand registries with ^{13}CO-labeled HFP in the middle strand. Each row of panels e−h has three-strand registries that were each a combination of two registries labeled by specific t_1 and t_2, which denote the t of the top/middle and middle/bottom strands, respectively. As with the fully constrained models, the registries in each column of panels e−h corresponded to a particular ^{13}CO HFP/^{15}N HFP arrangement with label $v = 1$, 2, 3, or 4, respectively. The ^{13}CO HFP:^{15}N HFP population ratio of 1:2 correlated with a sum weighting of 1/9 for the $v = 1$ registries with individual registry weighting $w_1 = 1/(9 \times 9) = 1/81$. The sum weightings for $v = 2$, 3, and 4 were 2/9, 2/9, and 4/9, respectively, with individual weightings $w_2 = 2/81$, $w_3 = 2/81$, and $w_4 = 4/81$, respectively. Equation 11 was modified for the unconstrained model:

$$S_{1u}^{lab}(\tau) = \sum_{t_1=1}^{3} \sum_{t_2=1}^{3} \left\{ f_{t_1} f_{t_2} \sum_{v=1}^{4} \left[w_v \gamma_{1t_1t_2uv}^{lab}(\tau) \right] \right\} \times S_0^{lab}(\tau) \quad (13)$$

Similar to the fully constrained model, many combinations of t_1, t_2, u, and v have an r_{CN} of > 7 Å with consequent $d_{CN} \approx 0$ and $\gamma_{1t_1t_2uv}^{lab}(\tau) = 1$. In Figure 5e−g, such registries are not enclosed by a box. Similar to results for the fully constrained model, the $\gamma_{1t_1t_2uv}^{lab}(\tau)$ values were similar for the two antiparallel registries, and an average value was used.

The values of f_1, f_2, and f_3 in the unconstrained model were the same for the HFP-P, HFP-A, and HFP-AP samples with $f_3 = 1 - f_1 - f_2$. Best-fit values of f_1 and f_2 were obtained with eq 12, and Figure 6b displays a plot of χ^2 versus f_1 and f_2 with a best-fit f_1 of 0.11 and a best-fit f_2 of 0.46 and a corresponding χ^2_{min} of 8. The unconstrained model was reasonable as evidenced by a best-fit χ^2 that was smaller than the number of degrees of fitting, 19. Similar to the results of the fully

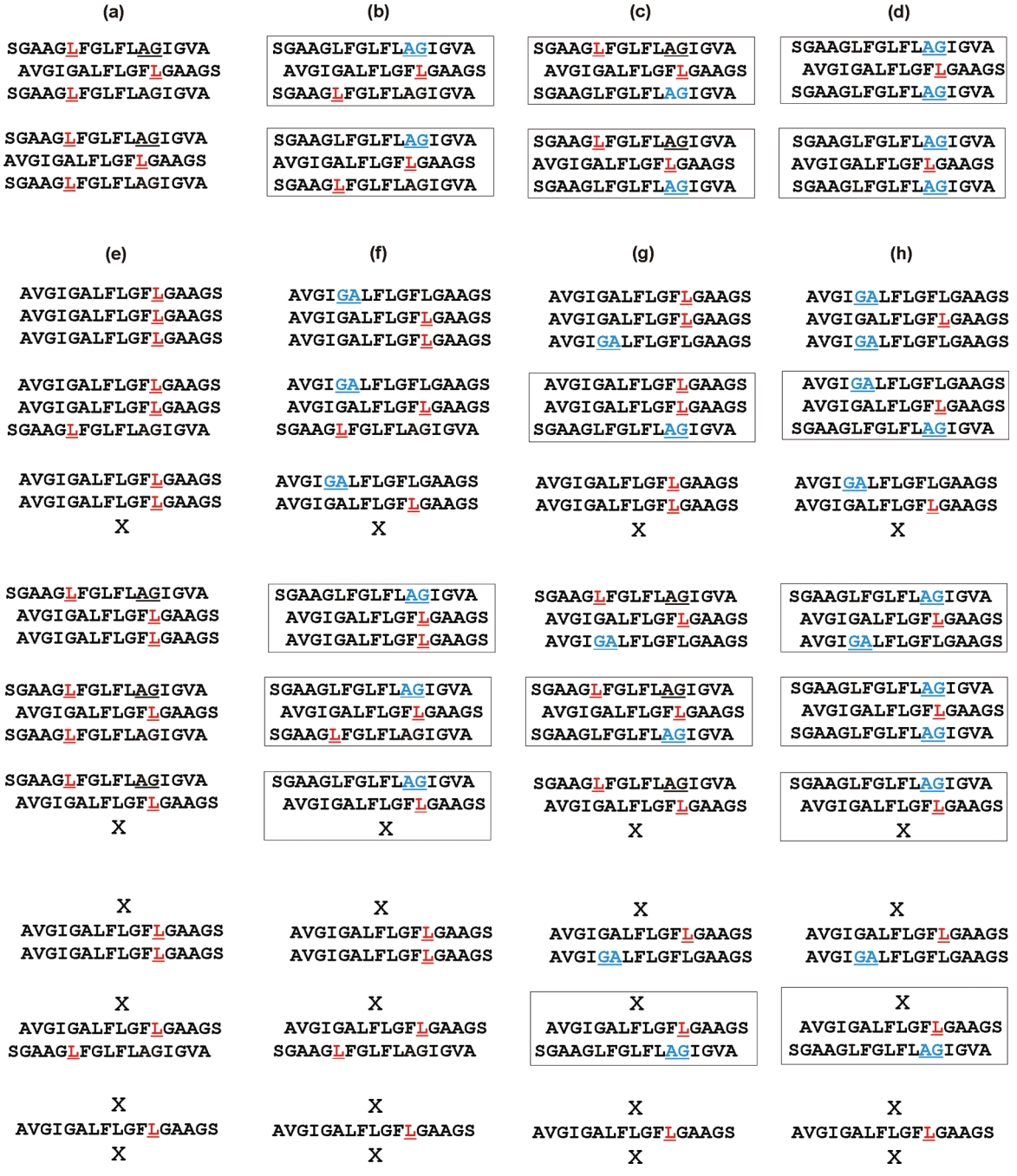

FIGURE 5: Schematics of three adjacent HFPs for HFP-A, i.e., $u = 2$, in (a−d) fully constrained or (e−h) unconstrained models. Red and blue denote ^{13}CO- and ^{15}N-labeled residues, respectively, and the labeled ^{13}CO in the middle strand was hydrogen bonded to the HN group of the residue in the top strand. Panels a−d display antiparallel 16→1/1→16 (top) or 17→1/1→17 (bottom) registries, while panels e−h display parallel 1→17/1→17, antiparallel 16→1/1→16, and X registries, where X refers to a registry for which the labeled r_{CN} value is >7 Å, i.e., beyond the approximate detection limit of the SSNMR experiment, and which is not 1→17/1→17, 2→17/1→16, 16→1/1→16, or 17→1/1→17. Correspondence between columns and the index v are as follows: a and e, $v = 1$; b and f, $v = 2$; c and g, $v = 3$; d and h, $v = 4$. Both rows of three-strand arrangements in panels a−d correspond to $t = 2$, and the row, t_1, t_2 correspondence in panels e−h is as follows: row 1, $t_1 = 1$ and $t_2 = 1$; row 2, $t_1 = 1$ and $t_2 = 2$; row 3, $t_1 = 1$ and $t_2 = 3$; row 4, $t_1 = 2$ and $t_2 = 1$; row 5, $t_1 = 2$ and $t_2 = 2$; row 6, $t_1 = 2$ and $t_2 = 3$; row 7, $t_1 = 3$ and $t_2 = 1$; row 8, $t_1 = 3$ and $t_2 = 2$; row 9, $t_1 = 3$ and $t_2 = 3$. For each three-strand arrangement enclosed by a box, the $\gamma^{lab}_{1tuv}(\tau)$ or $\gamma_{1t_1t_2uv}^{lab}(\tau)$ values were calculated by SIMPSON simulation. For arrangements with t, t_1, or $t_2 = 2$, fitting to experiment was based on γ values that were the average of those calculated with 16→1/1→16 and 17→1/1→17 registries, although the latter registry is not displayed in panels e−h. For any arrangement not enclosed by a box, $\gamma^{lab}_{1tuv}(\tau) = 1$ or $\gamma_{1t_1t_2uv}^{lab}(\tau) = 1$.

constrained model, the f_1 fractional parallel population was small and the f_2 antiparallel population and $f_3 \approx 0.4$ other population were significant.

This unconstrained model fitting was done with nad calculated with a long-range model and half-min β and half-max β structure. Similar to those of the fully constrained model, best-fit f_1, f_2, and χ^2 values for the unconstrained model were (1) negligibly affected by the structural distribution of the long-range nad model and (2) significantly increased by use of a short-range nad model.

DISCUSSION

This paper sets an upper limit of ~0.15 on the fraction of membrane-associated HFP in in-register parallel β sheet structure, and this result is supported by both qualitative analysis of the

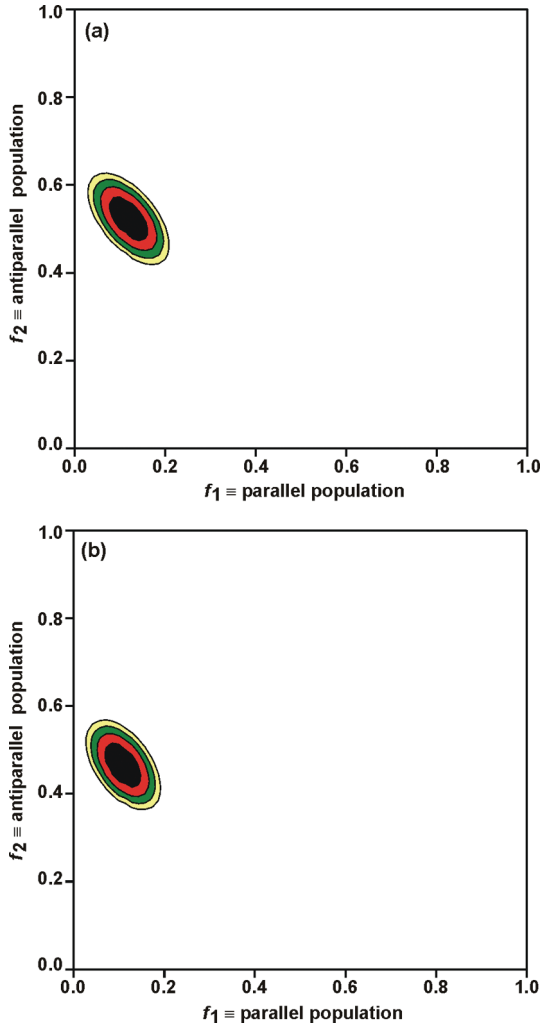

FIGURE 6: Contour plots of χ^2 vs f_1 parallel and f_2 antiparallel fractional populations for (a) fully constrained and (b) unconstrained models. In each plot, f_1 is the sum of populations of 1→17/1→17 and 2→17/1→16 parallel registries and f_2 is the sum of populations of 16→1/1→16 and 17→1/1→17 antiparallel registries. For plot a, the best-fit values were as follows: $f_1 = 0.12 \pm 0.03$, $f_2 = 0.52 \pm 0.04$, and $\chi^2_{min} = 11$. For plot b, the best-fit values were as follows: $f_1 = 0.11 \pm 0.03$, $f_2 = 0.46 \pm 0.04$, and $\chi^2_{min} = 8$. Parameter uncertainties were determined by the region of χ^2 within ~3 units of χ^2_{min}. In plot a, the black, red, green, yellow, and white regions correspond to the $\chi^2 < 14$, $14 < \chi^2 < 17$, $17 < \chi^2 < 20$, $20 < \chi^2 < 23$, and $\chi^2 > 23$ relationships, respectively, and in plot b, the regions correspond to the $\chi^2 < 11$, $11 < \chi^2 < 14$, $14 < \chi^2 < 17$, $17 < \chi^2 < 20$, and $\chi^2 > 20$ relationships, respectively.

data (Figure 3b) and quantitative analyses with fully constrained and unconstrained models (Figure 6). Both models fit the data well and yielded similar best-fit fractional populations of parallel registries and similar populations of antiparallel registries. The small fractional parallel population agrees with some earlier SSNMR studies but differs from interpretations of other SSNMR and IR data that reported ~0.5 and ~1.0 fractions of in-register parallel structure, respectively (*27*, *30*−*32*). Our study used samples with sparse isotopic labeling, while the earlier studies interpreted to support a large fraction of parallel structure used samples with extensive labeling. We think that there was ambiguity of interpretation in the studies of extensively labeled samples and that the data could also be reasonably interpreted in terms of small in-register parallel populations. For example, the earlier SSNMR study also used the REDOR technique but with only a single τ (24 ms) and with samples containing equimolar amounts of HFP labeled with ^{13}CO on three sequential residues and HFP labeled with ^{15}N on three sequential residues. The typical $(\Delta S/S_0)^{exp}$ was ~0.1 and approximately independent of the positions of the labeled residues and also had some contribution from nad. It was not possible to conduct unambiguous quantitative analysis of registry distributions because (1) each sample was extensively labeled so that a non-zero $\Delta S/S_0$ was expected for many different registries, (2) $(\Delta S/S_0)^{exp}$ values were only measured for a single τ, and (3) a "HFP-NC"-type sample was not studied and nad was therefore not quantitatively modeled.

The samples for the IR study were also extensively labeled with backbone ^{13}CO groups at either (1) A1 to V3, G5 to L9; (2) F8 to G16; or (3) A1 to V3, G5 to G16. The authors' interpretation of their spectra to support predominant in-register parallel structure was based in part on expected effects of (^{13}C═^{16}O electric dipole)···(^{13}C═^{16}O electric dipole) coupling on the ^{13}C═O vibrational wavenumber and intensity. However, their interpretation appeared to neglect the substantial intramolecular coupling between ^{13}C═O bonds on adjacent residues, and we note that this coupling is independent of registry. In addition to these "undiluted" samples, three "diluted" samples were studied that had an equimolar mixture of a labeled and unlabeled peptide. The wavenumber (ν) of a ^{13}C═^{16}O vibration is sensitive to nearby (~5 Å distant) C═O vibrations and is higher with ^{12}C═^{16}O neighbors than with ^{13}C═^{16}O neighbors. If there is hydrogen bonding between ^{13}CO-labeled residues of adjacent strands in an undiluted sample, the corresponding diluted sample should have an increased fraction of ^{13}C═O/^{12}C═O proximities and a decreased fraction of ^{13}C═O/^{13}C═O proximities, and $\Delta\nu = \nu_{diluted} - \nu_{undiluted} > 0$. If there were a major fraction of parallel 1→17/1→17 structure (as claimed by the authors), dilution of (1) A1-V3, G5-L9; (2) F8-G16; or (3) A1-V3, G5-G16 labeled HFPs would have had a comparable effect on proximities and resulted in similar $\Delta\nu$ values. However, the experimental $\Delta\nu_{A1\text{-}V3,G5\text{-}L9} \approx \Delta\nu_{F8\text{-}G16} \approx \Delta\nu_{A1\text{-}V3,G5\text{-}G16}/2$ relationship is inconsistent with a large fraction of in-register parallel structure. Like the earlier SSNMR study on extensively labeled samples, extensive labeling of the IR samples also meant that the IR data were consistent with many registry distributions and precluded more quantitative analysis of the distribution. Overall, the sparse labeling of our SSNMR study allowed for much more unambiguous and quantitative determination of the populations of specific registries. This general approach can be applied in the future to determine the registry distributions of HFP constructs with very high or low fusogenicity such as HFPtr or the V2E mutant, respectively.

Figure 7 displays a structure−function model for HFP based on results from this study and earlier studies. Prior to membrane binding, HFP is monomeric in aqueous solution and has random coil structure (*11*, *12*, *18*). HFP sequentially (1) binds to membranes, (2) forms β sheet oligomers with a significant fraction of 16→1/1→16 and 17→1/1→17 antiparallel registries, and (3) induces membrane fusion as monitored by intervesicle lipid mixing (*12*, *14*, *17*, *18*). It is also known that the A6 and L9 residues of β sheet HFP insert shallowly into the membrane with correlation between membrane insertion depth and both membrane perturbation and fusion rate (*19*, *36*, *49*). A global structure−function model holds that nontransmembrane HFP insertion perturbs bilayer structure and moves the membrane on the fusion reaction coordinate toward the highly perturbed transition state with a consequent reduction in fusion activation energy and an increase in fusion rate.

There is functional and electron microscopic evidence that multiple gp41 trimers are required for fusion, and Figure 7(right)

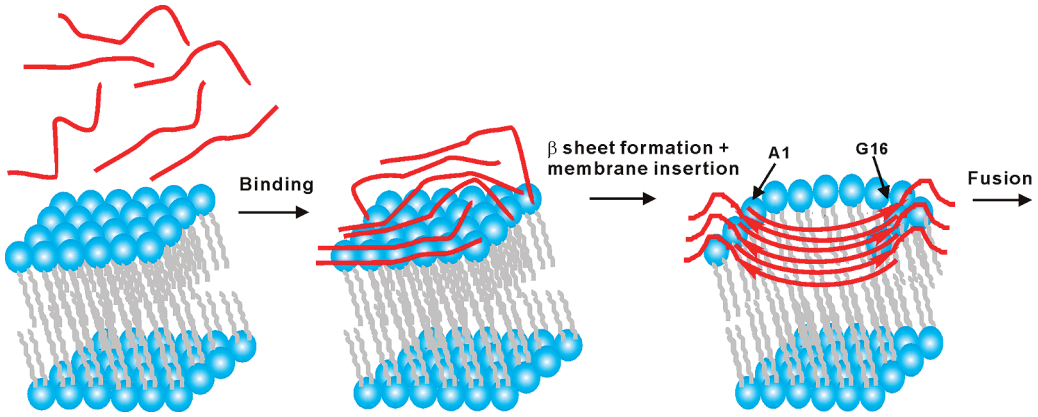

FIGURE 7: Pictorial model of HFP (red lines) binding to membranes followed by antiparallel β sheet formation and membrane insertion and then fusion. Time increases from left to right. For the sake of clarity, some lipids are not shown in the right-most picture. Although there are no data yet on fusion peptide structure during HIV−host cell fusion, the antiparallel β sheet structure of the right-most picture is plausible because (1) the structure is consistent with multiple trimers at the fusion site and (2) the structure is membrane-inserted with deeper insertion positively correlated with greater membrane perturbation and an increased vesicle fusion rate.

shows a β sheet HFP hexamer as would be reasonable for interleaved antiparallel fusion peptides from two gp41 trimers. While there are no data specifically supporting a HFP hexamer, HFP β sheet oligomers likely contain a small number of molecules because for ~90% of HFP molecules, there is (1) an A1 ^{13}CO−lipid ^{31}P distance of ~5 Å, i.e., close contact of most HFPs with the membrane, and (2) significant temperature dependence of intensities of SSNMR spectra (*19*, *26*). Interleaved antiparallel fusion peptides from multiple gp41 trimers may also be the fusogenic structure of HIV−host cell fusion. As noted above, this structure can insert into and perturb membranes, which are likely requirements for HIV−host cell fusion.

The experimentally observed membrane insertion of the central β sheet region (e.g., A6−L12) of HFP is consistent with a $\Delta G^{\text{insertion}}$ of approximately −6 kJ/mol for the fully constrained 17→1/1→17 registry as calculated by summing individual residue insertion energies for the L12→A6/A6→L12 registry (Figure 1c) (*50*). A similar calculation yielded a $\Delta G^{\text{insertion}}$ of approximately −3 kJ/mol for L12→G5/G5→L12 of the 16→1/1→16 registry. The $\Delta G^{\text{insertion}}$ of approximately −6 kJ/mol for A6→L12/A6→L12 of the 1→17/1→17 parallel registry suggests that $\Delta G^{\text{insertion}}$ does not underlie the preference for antiparallel structure over parallel structure. This preference may instead be due to $\Delta G^{\text{electrostatic}}$ as the HFP N-terminus is located in the high-water content lipid headgroup region and is therefore likely protonated. The shortest intermolecular NH_3^+−NH_3^+ distance is ~5 Å for the insignificantly populated 1→17/1→17 registry and ~10 Å for the significantly populated 17→1/1→17 registry. When $\varepsilon_{\text{dielectric}} = 78$ and for hexameric HFP, $\Delta G^{\text{electrostatic}}$ is ≈5.1 kJ/mol for the 1→17/1→17 registry and ≈1.5 kJ/mol for the 17→1/1→17 registry.

We expect that inclusion of the non-native C-terminal W(K)$_6$A tag does not contribute to the preference for antiparallel over parallel registry because either registry would have similar minimized electrostatic repulsion energy. Such repulsion would be minimized by (1) extensive solvation of the tag and (2) large intertag distances that are possible because of random coil tag structure. Tag solvation is supported by the previously observed lack of membrane insertion of HFP beyond residue L12, and random coil tag structure is supported by broad NMR line widths in the C-terminal region of HFP (*14*, *19*). We also note that inclusion of the tag has a minor effect on fusion activity and that similar REDOR $\Delta S/S_0$ values were observed for mixtures of triply ^{13}CO- and ^{15}N-labeled HFPs with or without the tag (*12*, *27*).

In contrast to the reasonably large distribution of membrane-associated HFP registries, i.e., significant 16→1/1→16, 17→1/1→17, and X registries, SSNMR studies of β sheet registries of the protein in amyloid fibrils have typically shown a single registry that is usually in-register parallel, e.g., 1→17/1→17 (*28*, *29*). The width of a fibril is at most a few protein molecules, and the length is > 200 molecules and along the intermolecular β sheet hydrogen bonding direction. The amyloid fibrils are grown in aqueous solution (without lipid), and their greater registry homogeneity may reflect ordered fibril growth from seeds (*51*).

One distinctive feature of this study is the development of a quantitative nad model that was experimentally validated. Accurate fitting of the HFP-NC data and fitting of the membrane-associated HFP data relied on a long-range nad model that included effects of na nuclei < 7 Å from each labeled nucleus. For this model, the nad was approximately independent of secondary and tertiary structure. The nad was systematically underestimated by a short-range model that considered only na nuclei separated by one or two bonds from each labeled nucleus.

ACKNOWLEDGMENT

NMR and mass spectra were obtained at Michigan State University facilities. We acknowledge useful discussions with Dr. Wei Qiang, Dr. Kelly Sackett, and Dr. Charles Gabrys.

SUPPORTING INFORMATION AVAILABLE

Table of $(\Delta S/S_0)^{\text{exp}}$ values and schematics of spin geometries and associated $\gamma^{\text{lab}}_{1tuv}(\tau)$ or $\gamma^{\text{lab}}_{1t_1t_2uv}(\tau)$ calculated by SIMPSON simulation. This material is available free of charge via the Internet at http://pubs.acs.org.

REFERENCES

1. White, J. M., Delos, S. E., Brecher, M., and Schornberg, K. (2008) Structures and mechanisms of viral membrane fusion proteins: Multiple variations on a common theme. *Crit. Rev. Biochem. Mol. Biol. 43*, 189–219.
2. Tan, K., Liu, J., Wang, J., Shen, S., and Lu, M. (1997) Atomic structure of a thermostable subdomain of HIV-1 gp41. *Proc. Natl. Acad. Sci. U.S.A. 94*, 12303–12308.
3. Caffrey, M., Cai, M., Kaufman, J., Stahl, S. J., Wingfield, P. T., Covell, D. G., Gronenborn, A. M., and Clore, G. M. (1998) Three-dimensional solution structure of the 44 kDa ectodomain of SIV gp41. *EMBO J. 17*, 4572–4584.

4. Yang, Z. N., Mueser, T. C., Kaufman, J., Stahl, S. J., Wingfield, P. T., and Hyde, C. C. (1999) The crystal structure of the SIV gp41 ectodomain at 1.47 Å resolution. *J. Struct. Biol. 126*, 131–144.
5. Buzon, V., Natrajan, G., Schibli, D., Campelo, F., Kozlov, M. M., and Weissenhorn, W. (2010) Crystal structure of HIV-1 gp41 including both fusion peptide and membrane proximal external regions. *PLoS Pathog. 6*, e1000880.
6. Freed, E. O., Myers, D. J., and Risser, R. (1990) Characterization of the fusion domain of the human immunodeficiency virus type 1 envelope glycoprotein gp41. *Proc. Natl. Acad. Sci. U.S.A. 87*, 4650–4654.
7. Freed, E. O., Delwart, E. L., Buchschacher, G. L., Jr., and Panganiban, A. T. (1992) A mutation in the human immunodeficiency virus type 1 transmembrane glycoprotein gp41 dominantly interferes with fusion and infectivity. *Proc. Natl. Acad. Sci. U.S.A. 89*, 70–74.
8. Durell, S. R., Martin, I., Ruysschaert, J. M., Shai, Y., and Blumenthal, R. (1997) What studies of fusion peptides tell us about viral envelope glycoprotein-mediated membrane fusion. *Mol. Membr. Biol. 14*, 97–112.
9. Nieva, J. L., and Agirre, A. (2003) Are fusion peptides a good model to study viral cell fusion? *Biochim. Biophys. Acta 1614*, 104–115.
10. Epand, R. M. (2003) Fusion peptides and the mechanism of viral fusion. *Biochim. Biophys. Acta 1614*, 116–121.
11. Chang, D. K., Chien, W. J., and Cheng, S. F. (1997) The FLG motif in the N-terminal region of glucoprotein 41 of human immunodeficiency virus type 1 adopts a type-I β turn in aqueous solution and serves as the initiation site for helix formation. *Eur. J. Biochem. 247*, 896–905.
12. Yang, J., Prorok, M., Castellino, F. J., and Weliky, D. P. (2004) Oligomeric β-structure of the membrane-bound HIV-1 fusion peptide formed from soluble monomers. *Biophys. J. 87*, 1951–1963.
13. Pereira, F. B., Goni, F. M., Muga, A., and Nieva, J. L. (1997) Permeabilization and fusion of uncharged lipid vesicles induced by the HIV-1 fusion peptide adopting an extended conformation: Dose and sequence effects. *Biophys. J. 73*, 1977–1986.
14. Yang, J., Gabrys, C. M., and Weliky, D. P. (2001) Solid-state nuclear magnetic resonance evidence for an extended β strand conformation of the membrane-bound HIV-1 fusion peptide. *Biochemistry 40*, 8126–8137.
15. Qiang, W., Bodner, M. L., and Weliky, D. P. (2008) Solid-state NMR spectroscopy of human immunodeficiency virus fusion peptides associated with host-cell-like membranes: 2D correlation spectra and distance measurements support a fully extended conformation and models for specific antiparallel strand registries. *J. Am. Chem. Soc. 130*, 5459–5471.
16. Brugger, B., Glass, B., Haberkant, P., Leibrecht, I., Wieland, F. T., and Krasslich, H. G. (2006) The HIV lipidome: A raft with an unusual composition. *Proc. Natl. Acad. Sci. U.S.A. 103*, 2641–2646.
17. Buzon, V., Padros, E., and Cladera, J. (2005) Interaction of fusion peptides from HIV gp41 with membranes: A time-resolved membrane binding, lipid mixing, and structural study. *Biochemistry 44*, 13354–13364.
18. Yang, R., Prorok, M., Castellino, F. J., and Weliky, D. P. (2004) A trimeric HIV-1 fusion peptide construct which does not self-associate in aqueous solution and which has 15-fold higher membrane fusion rate. *J. Am. Chem. Soc. 126*, 14722–14723.
19. Qiang, W., Sun, Y., and Weliky, D. P. (2009) A strong correlation between fusogenicity and membrane insertion depth of the HIV fusion peptide. *Proc. Natl. Acad. Sci. U.S.A. 106*, 15314–15319.
20. Yang, X. Z., Kurteva, S., Ren, X. P., Lee, S., and Sodroski, J. (2005) Stoichiometry of envelope glycoprotein trimers in the entry of human immunodeficiency virus type 1. *J. Virol. 79*, 12132–12147.
21. Magnus, C., Rusert, P., Bonhoeffer, S., Trkola, A., and Regoes, R. R. (2009) Estimating the stoichiometry of human immunodeficiency virus entry. *J. Virol. 83*, 1523–1531.
22. Sougrat, R., Bartesaghi, A., Lifson, J. D., Bennett, A. E., Bess, J. W., Zabransky, D. J., and Subramaniam, S. (2007) Electron tomography of the contact between T cells and SIV/HIV-1: Implications for viral entry. *PLoS Pathog. 3*, 571–581.
23. Lau, W. L., Ege, D. S., Lear, J. D., Hammer, D. A., and DeGrado, W. F. (2004) Oligomerization of fusogenic peptides promotes membrane fusion by enhancing membrane destabilization. *Biophys. J. 86*, 272–284.
24. Pan, J. H., Lai, C. B., Scott, W. R. P., and Straus, S. K. (2010) Synthetic fusion peptides of tick-borne Encephalitis virus as models for membrane fusion. *Biochemistry 49*, 287–296.
25. Han, X., and Tamm, L. K. (2000) A host-guest system to study structure-function relationships of membrane fusion peptides. *Proc. Natl. Acad. Sci. U.S.A. 97*, 13097–13102.
26. Bodner, M. L., Gabrys, C. M., Parkanzky, P. D., Yang, J., Duskin, C. A., and Weliky, D. P. (2004) Temperature dependence and resonance assignment of ^{13}C NMR spectra of selectively and uniformly labeled fusion peptides associated with membranes. *Magn. Reson. Chem. 42*, 187–194.
27. Yang, J., and Weliky, D. P. (2003) Solid state nuclear magnetic resonance evidence for parallel and antiparallel strand arrangements in the membrane-associated HIV-1 fusion peptide. *Biochemistry 42*, 11879–11890.
28. Benzinger, T. L., Gregory, D. M., Burkoth, T. S., Miller-Auer, H., Lynn, D. G., Botto, R. E., and Meredith, S. C. (1998) Propagating structure of Alzheimer's β-amyloid(10−35) is parallel β-sheet with residues in exact register. *Proc. Natl. Acad. Sci. U.S.A. 95*, 13407–13412.
29. Tycko, R. (2006) Molecular structure of amyloid fibrils: Insights from solid-state NMR. *Q. Rev. Biophys. 39*, 1–55.
30. Zheng, Z., Yang, R., Bodner, M. L., and Weliky, D. P. (2006) Conformational flexibility and strand arrangements of the membrane-associated HIV fusion peptide trimer probed by solid-state NMR spectroscopy. *Biochemistry 45*, 12960–12975.
31. Zheng, Z., Qiang, W., and Weliky, D. P. (2007) Investigation of finite-pulse radiofrequency-driven recoupling methods for measurement of intercarbonyl distances in polycrystalline and membrane-associated HIV fusion peptide samples. *Magn. Reson. Chem. 245*, S247–S260.
32. Sackett, K., and Shai, Y. (2005) The HIV fusion peptide adopts intermolecular parallel β-sheet structure in membranes when stabilized by the adjacent N-terminal heptad repeat: A ^{13}C FTIR study. *J. Mol. Biol. 350*, 790–805.
33. Lapatsanis, L., Milias, G., Froussios, K., and Kolovos, M. (1983) Synthesis of N-2,2,2-(trichloroethoxycarbonyl)-L-amino acids and N-(9-fluorenylmethoxycarbonyl)-L-amino acids involving succinimidoxy anion as a leaving group in amino-acid protection. *Synthesis 8*, 671–673.
34. Siminovitch, D. J., Ruocco, M. J., Makriyannis, A., and Griffin, R. G. (1987) The effect of cholesterol on lipid dynamics and packing in diether phosphatidylcholine bilayers. X-ray diffraction and ^{2}H-NMR study. *Biochim. Biophys. Acta 901*, 191–200.
35. Komatsu, H., and Rowe, E. S. (1991) Effect of cholesterol on the ethanol-induced interdigitated gel phase in phosphatidylcholine: Use of fluorophore pyrene-labeled phosphatidylcholine. *Biochemistry 30*, 2463–2470.
36. Gabrys, C. M., Yang, R., Wasniewski, C. M., Yang, J., Canlas, C. G., Qiang, W., Sun, Y., and Weliky, D. P. (2010) Nuclear magnetic resonance evidence for retention of a lamellar membrane phase with curvature in the presence of large quantities of the HIV fusion peptide. *Biochim. Biophys. Acta 1798*, 194–201.
37. Huster, D., Xiao, L. S., and Hong, M. (2001) Solid-state NMR investigation of the dynamics of the soluble and membrane-bound colicin Ia channel-forming domain. *Biochemistry 40*, 7662–7674.
38. Gullion, T., and Schaefer, J. (1989) Rotational-echo double-resonance NMR. *J. Magn. Reson. 81*, 196–200.
39. Gullion, T., Baker, D. B., and Conradi, M. S. (1990) New, compensated Carr-Purcell sequences. *J. Magn. Reson. 89*, 479–484.
40. Bennett, A. E., Rienstra, C. M., Auger, M., Lakshmi, K. V., and Griffin, R. G. (1995) Heteronuclear decoupling in rotating solids. *J. Chem. Phys. 103*, 6951–6958.
41. Long, H. W., and Tycko, R. (1998) Biopolymer conformational distributions from solid-state NMR: α-Helix and 3_{10}-helix contents of a helical peptide. *J. Am. Chem. Soc. 120*, 7039–7048.
42. Fowler, D. J., Weis, R. M., and Thompson, L. K. (2010) Kinase-active signaling complexes of bacterial chemoreceptors do not contain proposed receptor-receptor contacts observed in crystal structures. *Biochemistry 49*, 1425–1434.
43. Bevington, P. R., and Robinson, D. K. (1992) Data Reduction and Error Analysis for the Physical Sciences, 2nd ed., McGraw-Hill, Boston.
44. Oas, T. G., Hartzell, C. J., McMahon, T. J., Drobny, G. P., and Dahlquist, F. W. (1987) The carbonyl ^{13}C chemical-shift tensors of 5 peptides determined from ^{15}N dipole-coupled chemical shift powder patterns. *J. Am. Chem. Soc. 109*, 5956–5962.
45. Bak, M., Rasmussen, J. T., and Nielsen, N. C. (2000) SIMPSON: A general simulation program for solid-state NMR spectroscopy. *J. Magn. Reson. 147*, 296–330.
46. Bak, M., Schultz, R., Vosegaard, T., and Nielsen, N. C. (2002) Specification and visualization of anisotropic interaction tensors in polypeptides and numerical simulations in biological solid-state NMR. *J. Magn. Reson. 154*, 28–45.
47. Jaroniec, C. P., Kaufman, J. D., Stahl, S. J., Viard, M., Blumenthal, R., Wingfield, P. T., and Bax, A. (2005) Structure and dynamics of micelle-associated human immunodeficiency virus gp41 fusion domain. *Biochemistry 44*, 16167–16180.

48. Zhang, H. Y., Neal, S., and Wishart, D. S. (2003) RefDB: A database of uniformly referenced protein chemical shifts. *J. Biomol. NMR 25*, 173–195.
49. Tristram-Nagle, S., Chan, R., Kooijman, E., Uppamoochikkal, P., Qiang, W., Weliky, D. P., and Nagle, J. F. (2010) HIV fusion peptide penetrates, disorders, and softens T-cell membrane mimics. *J. Mol. Biol. 402*, 139–153.
50. Hessa, T., Kim, H., Bihlmaier, K., Lundin, C., Boekel, J., Andersson, H., Nilsson, I., White, S. H., and Heijne, G. (2005) Recognition of tranmembrane helices by the endoplasmic reticulum translocon. *Nature 433*, 377–381.
51. Petkova, A. T., Leapman, R. D., Guo, Z. H., Yau, W. M., Mattson, M. P., and Tycko, R. (2005) Self-propagating, molecular-level polymorphism in Alzheimer's β-amyloid fibrils. *Science 307*, 262–265.